# Calculation of Restoring Moment in Ship roll motion through Numerical Simulation

S. S. Kianejad, *Australian Maritime College, Australia,* seyed.kianejadtejenaki@utas.edu.au

Hossein Enshaei, *Australian Maritime College, Australia,* hossein.enshaei@utas.edu.au

Jonathan Duffy, *Australian Maritime College, Australia,* j.duffy@utas.edu.au

Nazanin Ansarifard, *Australian Maritime College, Australia,* nazanin.ansarifard@utas.edu.au

**ABSTRACT**

Accurate calculation of restoring moment, virtual mass moment of inertia and damping moment increases accuracy of a ship's dynamic stability simulation. The current methods of approximating the roll restoring moment are based on hydrostatic calculations. These methods overlook dynamic conditions and the effects of pressure distribution around the body. In the current study, a CFD approach is adopted based on a harmonic excited roll motion method to investigate roll motion characteristics and calculate the restoring moment in dynamic conditions. This investigation considers multiple degrees of freedom (DOF) at different Froude numbers, bare-hull and fully appended conditions. The results show that the restoring moment in dynamic condition is larger than static condition.

***Keywords:*** *Restoring moment, damping moment, moment of inertia, CFD, harmonic excited roll motion.*

## 1. INTRODUCTION

A ship in the rough sea condition experiences non-linear translational and rotational motions. These motions change the performance of the ship, and decrease safety. There is a greater concern regarding roll motion compared to other motions because the damping and restoring moments which resist against the roll motion increment, are lower.

Capsizing of a ship can occur both in resonant and non-resonant conditions (Wawrzyński and Krata, 2016). The non-resonant capsizing can occur in two different situations; when a ship experiences a large roll motion in a seaway and is also acted upon by gusty wind, and in surf-riding and broaching phenomena. The external forces and moments induced by regular waves at a specific frequency can excite the resonance condition. Capsizing in the resonance condition can occur due to two different phenomena of synchronous and parametric roll, where the encounter frequency is equal and two times of the ship's natural roll frequency, respectively. The parametric roll is most probable to arise in some types of ships like container ship in head sea condition when the wavelength is equal to the ship length. While all ship types may be subjected to the synchronous rolling in beam sea conditions. This condition is very dangerous since, small external forces and moments can impose a large roll angle.

In order to investigate a ship's motions, there are generally three approaches including

experiments, CFD and equation based methods. Direct investigation of different failure modes of dynamic stability is time-consuming, therefore, most studies have been conducted using the equation based methods. The accuracy of these methods depends on several hydrodynamic coefficients like mass and added mass moment of inertia, damping and restoring. However, the magnitude and effects of restoring moment at resonance condition is much larger than the other parts. Thus, computing the precise magnitude of the restoring part is essential.

In this regard, Neves (2002), Neves et al. (2002), Holden et al. (2007) used a 3-DOF non-linear model to investigate the effects of heave, pitch and roll motions on the restoring moment. Although this model was simpler than 6-DOF, the computation time of forces and coupled motions was significant. Oh et al. (2000) found that the effects of heave and pitch motions on righting arm are small, hence modelling of the coupled heave, pitch and roll motions could be simplified. They used a 1-DOF model by adding the coupled heave and pitch motions effects on the restoring moment, which was approximated by a third order fitting polynomial equation. In the case of regular waves, Bulian et al. (2006) introduced a 1.5-DOF model based on a quasi-static approach, where the half DOF is related to the coupled heave and pitch motions. They estimated the righting arm at different angles based on the height and position of the wave crest regarding the ship's length using polynomial fitting function and Fourier series. In case of irregular waves, they introduced Grim's effective wave to estimate the righting moment which provides a conservative approximation. Vidic (2011), Dunwoody (1989) assumed a linear relation between changes of metacentric height (GM) of a ship in the calm water and wave conditions based on the wave height. Silva et al. (2005) proposed that the restoring moment can be predicted accurately by computing the pressure distribution over the wetted surface area, however, this requires long running simulations. They suggested a fifth-order nonlinear polynomial function instead of a direct calculation of the righting arm; however, it may not be feasible for some types of ships. Song et al. (2013) developed a 1-DOF method to predict the parametric roll that used a GM spectrum considering the coupled heave and pitch motions. The variation of righting arm was estimated by combining the righting arm in the calm water and the fluctuation of the GM. The GM spectrum was computed regarding the heave motion, pitch motion and wave elevation.

What is apparent according to the literature, a ship in the parametric roll and dead ship condition experiences the resonance condition where the roll angle increases over the time. The existing methods of predicting the restoring moment fail to take into account the influence of dynamic pressure on the ship's hull. Adding the dynamic pressure to the hydrostatic pressure improves calculation of the restoring moment in the dynamic conditions. To replicate the harmonic roll motion of a ship in these conditions, a harmonic excited roll motion (HERM) technique is used. In this study a model of a container ship is excited to compute the restoring moment using CFD simulations. Additionally, the effects of appendages, forward speed and number of degrees of freedom (DOF) on the roll restoring moments at a frequency close to the natural frequency of model are investigated.

## 2. SHIP GEOMETRY

A model of a Post-Panamax containership in bare and fully appended conditions was used. The appendages are rudder, propeller and bilge keels. The five bilge keels were installed on either side of the model in the middle section. The model was utilized for benchmarking at Hamburg ship model basin and more

information about the model can be found in (Moctar et al., 2012). A snapshot of the model is shown in Figure 1 and main particulars of the model and ship are presented in Table 1.

Table 1 Main characteristics of model and full-scale ship

| Main dimension | Full scale | Model |
|---|---|---|
| $L_{pp}$ [m] | 355 | 5.97 |
| $L_{wl}$ [m] | 360.91 | 6.07 |
| $B_{wl}$ [m] | 51 | 0.86 |
| D [m] | 14 | 0.24 |
| $C_B$ | 0.6544 | 0.65 |
| V [$m^3$] | 165868.5 | 0.79 |
| KM [m] | 25.05 | 0.42 |
| GM [m] | 1.37 | 0.02 |
| KG [m] | 23.68 | 0.39 |
| $T_0$ [s] | 38.17 | 4.95 |
| $I_{xx}$ [m] | 20.25 | 0.34 |
| $I_{yy}$ [m] | 88.19 | 1.48 |
| $I_{zz}$ [m] | 88.49 | 1.49 |

Figure 1 Hull geometry of the Post-Panamax container ship

## 3. NUMERICAL MODELLING

The present simulations were conducted by commercial RANS solver STAR-CCM+ and details of the selected approach are presented in the following sections. The model was excited in various conditions as presented in Table 2 to investigate the influence of several parameters on the roll motion characteristics. The fully appended (Full) and bare hull models were excited under a 25 Nm roll exciting moment at a frequency of 1.4 Rad/s and different Froude numbers (Fn.). The degrees of freedom (DOF) of the model was varied from only roll (R) motion to 6DOF. In the Table 2 heave, pitch and sway motions are shown by H, P and S, respectively.

Table 2 Test conditions to calculate the restoring moment in dynamic condition.

| Case No. | Fn. | Excitation frequency (Rad/s) | DOF | Model condition | Roll exciting moment (Nm) |
|---|---|---|---|---|---|
| 1 | 0 | 1.4 | R | Full | 25 |
| 2 | 0 | 1.4 | RH | Full | 25 |
| 3 | 0 | 1.4 | RP | Full | 25 |
| 4 | 0 | 1.4 | RS | Full | 25 |
| 5 | 0 | 1.4 | 6DOF | Full | 25 |
| 6 | 0 | 1.4 | 6DOF | Bare | 25 |
| 7 | 0.1 | 1.4 | R | Full | 25 |
| 8 | 0.1 | 1.4 | RH | Full | 25 |
| 9 | 0.1 | 1.4 | RP | Full | 25 |
| 10 | 0.1 | 1.4 | RS | Full | 25 |
| 11 | 0.1 | 1.4 | 6DOF | Full | 25 |
| 12 | 0.1 | 1.4 | 6DOF | Bare | 25 |
| 13 | 0.19 | 1.4 | R | Full | 25 |
| 14 | 0.19 | 1.4 | RH | Full | 25 |
| 15 | 0.19 | 1.4 | RP | Full | 25 |
| 16 | 0.19 | 1.4 | RS | Full | 25 |
| 17 | 0.19 | 1.4 | 6DOF | Full | 25 |
| 18 | 0.19 | 1.4 | 6DOF | Bare | 25 |

### 3.1 Governing equations and physics modelling

The incompressible averaged continuity and momentum equations in terms of tensor form and based on Cartesian coordinates were adopted to conduct simulations as follows (Ferziger et al., 1997):

$$\frac{\partial(\rho\bar{u}_i)}{\partial x_i} = 0 \tag{1}$$

$$\frac{\partial(\rho\bar{u}_i)}{\partial t} + \frac{\partial}{\partial x_j}(\rho\bar{u}_i\bar{u}_j + \rho\overline{u_i'u_j'}) = -\frac{\partial\bar{p}}{\partial x_i} + \frac{\partial\bar{\tau}_{ij}}{\partial x_j} \tag{2}$$

$$\bar{\tau}_{ij} = \mu\left(\frac{\partial\bar{u}_i}{\partial x_j} + \frac{\partial\bar{u}_j}{\partial x_i}\right) \tag{3}$$

The indices of i and j determine the flow direction of x and y-axes. ρ and μ are density and viscosity, $\bar{\tau}_{ij}$ and $\rho\overline{u_i'u_j'}$ reflect the mean viscous stress tensor and the mean Reynolds

stress tensor, respectively. $\overline{u}_i$ and $\overline{P}$ demonstrate the time-averaged velocity and pressure. The solver uses finite volume method to simulate the flow around the model and to link the continuity and momentum equations utilizes a predictor-corrector method. The realizable k–ε turbulence model was adopted to reduce the uncertainty of the stress tensor. This type of turbulence model is precise and economical in terms of time compared to other types of turbulence models (Tezdogan et al., 2015). In order to capture the free surface changes, the "volume of fluid" (VOF) was adopted and mesh size at that region was reduced to solve the interface between two phases of the water and air. The solver uses a segregated flow model to solve the continuity and momentum equations in an uncoupled condition and the second order upwind scheme and the Simple algorithm was utilized to discretize the governing equations. The dynamic fluid body interaction (DFBI) approach was employed to consider the effects of forces on the model like a real sea condition. Courant number (CFL) was used to determine the time step. The magnitude of Courant number was selected less than one for each cell to have numerical stability.

### 3.2 Meshing structure

An overset mesh method was used to simulate the model motions. It includes the overset and a background region. The overset region is connected to the model and has motions in the same direction of the model inside of a stationary background region (Field, 2013). The cell size of the overset region was set small enough to capture the flow separation, eddy, boundary layer and wave generation over harmonic roll motion. Four types of meshers were used to generate the mesh including trimmed, prism layer, surface and automatic surface repair. The trimmed mesher was used to generate high-quality mesh and the prism layer was utilized to create perpendicular prismatic cells close to the model surface to capture the velocity changes and boundary layer. Three volumetric control zones were considered to reduce the size of cells, especially around the model and free surface to resolve sophisticated flow characteristics. An overlap volumetric control zone was used to match the cell size in the background and overset regions and minimize the possibility of solution divergence. An illustrations of the computational mesh are shown in Figure 2.

### 3.3 Boundary and initial conditions

Proper selection of the initial and boundary conditions reduces the simulation time and increases precision of the results. The upstream, top, bottom and lateral boundaries were set as velocity inlet, while the outlet boundary was set as pressure outlet to prevent any backflow. Determining the lateral, top and bottom boundaries as velocity inlet removes the velocity gradient due to the interaction between the walls and flow and directs the current towards the outlet boundary condition. Therefore, using such boundary conditions reduces the size of the flow domain. The magnitude of velocity for both the initial and boundary conditions was set according to the flat wave condition. The initial outlet boundary was set as hydrostatic pressure.

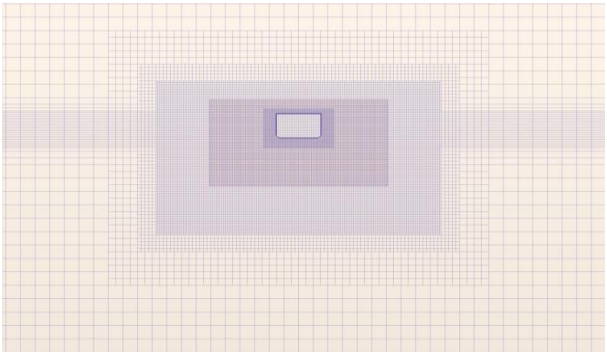

Figure 2 Cross section of the computation mesh

### 3.4 Methodology

The roll motion equation of a ship is governed by Newton's second law:

$$(I_{44}+\delta I_{44})\frac{\partial^2\varphi}{\partial t^2}+N_{44}\frac{\partial\varphi}{\partial t}+S_{44}\varphi=M_{E44}(t) \qquad (4)$$

Where the roll mass and added mass moment of inertia coefficients are $I_{44}$ and $\delta I_{44}$ respectively. $N_{44}$ is roll damping coefficient, $S_{44}$ reflects the roll restoring coefficient and $M_{E44}$ is an external roll exciting moment. Upon simulation of the fluid field around the body, exerted forces and moments on the body were computed in the earth-fixed coordinate system. The forces and moments were transferred into the body local coordinate system, which was set at the centre of gravity. In the following step, the velocity and acceleration of body were computed by solving the motion's equations and transferred back to the earth-fixed coordinate system to locate the body (Simonsen et al., 2013). For a range of frequencies lower and close to the resonance frequency, the exciting moment and the virtual roll moment of inertia (mass moment plus added mass moment of inertia) contribute to increase the roll motion, while the damping and restoring moments oppose the roll motion. Whereas, for a range of frequencies higher than the resonance frequency and at large roll angles the actions of these terms are different. The exciting moment at high frequency acts on the model quicker, which means that when the model experiences a larger roll angle, the exciting moment acts in a reverse direction due to the large generated phase shift between the roll motion and exciting moment. Therefore, the restoring, damping and exciting moments oppose the moment of inertia to reduce the roll angle.

The excitation frequency is very close to the natural roll frequency of model (the natural frequency of the model is 1.38 Rad/s). By computing the virtual mass moment of inertia based on (Kianejad et al., 2017), damping moment by (Handschel and Abdel-Maksoud, 2014) and knowing the exciting moment over different roll angles, the restoring moment is extracted. According to Kianejad's method, the angular acceleration is maximized at a maximum roll angle while the angular velocity is zero (damping moment will be negligible), the added mass moment of inertia is calculated by the equation below:

$$\delta I_{44}=\frac{M_{E44}(t)-S_{44}\varphi}{\frac{\partial^2\varphi}{\partial t^2}}-I_{44} \qquad (5)$$

Where, the restoring moment was calculated from the hydrostatic calculation and considering a quasi static condition at the maximum roll angle. The mass moment of inertia is the model characteristic and the acceleration is calculated by the simulations. The damping moments were computed based on the energy conservation method independently using harmonic excited roll motion (HERM) technique (Handschel and Abdel-Maksoud, 2014). In one cycle of the roll motion where the start-up effects are vanished, the work done by the exciting moment is equal to the dissipated damping energy, and the roll damping can be calculated by equation below:

$$N_{44}\frac{\partial\varphi}{\partial t}=\frac{M_{E44}(t)\sin\vartheta}{\omega\varphi_a}\frac{\partial\varphi}{\partial t} \qquad (6)$$

Where $\omega$ is frequency and $\varphi_a$ is maximum roll angle over one cycle of the roll motion. $\vartheta$ reflects the phase shift between the roll exciting moment and roll angle. Deducting damping, virtual mass moment of inertia terms from the exciting moment yields the residual moment, which is the restoring moment as follows:

$$S_{44}\varphi=M_{E44}(t)-(I_{44}+\delta I_{44})\frac{\partial^2\varphi}{\partial t^2}-N_{44}\frac{\partial\varphi}{\partial t} \qquad (7)$$

The numerical method was used to investigate the impact of effective parameters (different degrees of freedom, different Froude numbers and appendages) on the roll motion characteristics and hydrodynamic coefficients.

### 3.5 Mesh study

A mesh study was carried out for three mesh configurations to study the influence of each of them on the roll motion characteristics. In this section, the model was exposed to a 5.5 Nm roll exciting moment at a frequency of 1.39 Rad/s, which is close to the natural roll frequency of the model. The resistance of the model at a forward speed of 1.54 m/s was computed to choose the proper mesh configuration that could precisely calculate pressure and shear forces. The mesh configurations with 2.6, 3.6 and 5.8 million cells were considered. The increment for the cells was mainly focussed on the overset region to refine the quality of mesh. The initial and boundary conditions were the same while the number of mesh cells varied. The results of the simulations are compared with experimental data (Handschel and Abdel-Maksoud, 2014) shown in Table 3. The numerical simulations were performed considering the model free in 6DOF to replicate the physical model scale tests. Overall, the simulation results have larger values than the experimental values. It was found that the 5.8 million cells produces the most reliable results and provides the best correlation with the experimental data. The y+ value of the fine mesh configuration at Froude number 0.19 is 5 (**Error! Reference source not found.**). This magnitude of y+ and using realizable k–ε can reliably calculate shear forces on the model. The maximum roll angle and drag have 2.64% and 2.42% difference with experimental measurement, respectively. It shows this numerical approach has capability to simulate the roll motion accurately. Hence, it was used to simulate the roll motion characteristics in further simulations.

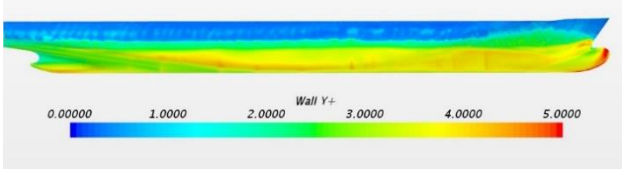


Figure 3 The y+ value of the model at Fn=0.19.

## 4. RESULTS AND DISCUSSION

### 4.1 Roll motion characteristics

The time histories of the roll, angular velocity, angular acceleration and roll moment for the bare and fully appended (Full) models are presented in

Figure 4 to Figure 7. The magnitude of exciting moment was 25 Nm at a frequency of 1.4 Rad/s where Froude number changes from 0 to 0.19. The fully appended model was simulated in different degrees of freedom (DOF) to investigate the effect of each degree on the roll motion characteristics. It can be seen in Figure 4 to Figure 7 that equipping the model with appendages and increasing the forward speed reduce the roll motion characteristics. Both appendages and forward speed increase the pressure difference between two sides of the hull and create a larger moment which impede the roll motion. The impact of appendages is more dominant at a larger roll angle because of the higher induced angular velocity and moment. Reduction of the maximum roll angle as a result of increasing the forward speed is depicted in Figure 4, and it is clear that reduction is more significant at Fn=0.19. At Froude number zero, considering the model free in only roll motion (R) experiences smaller roll motion characteristics, while increasing the DOF of the model such as being free in roll and heave (RH) slightly increases the roll motion characteristics. Considering the model free in roll and pitch (RP) and roll and sway (RS) conditions, increase the roll angle, however, the maximum roll angles

Table 3 Mesh convergence study and comparing by experimental measurement.

| | Exp. | 5.8 million | Difference | 3.6 million | Difference | 2.6 million | Difference |
|---|---|---|---|---|---|---|---|
| Roll | 14.42 | 14.8 | 2.64% | 15 | 4.02% | 15.7 | 8.88% |
| Roll Moment | - | 42.44 | - | 44.5 | - | 50 | - |
| Acceleration | - | 0.52 | - | 0.53 | - | 0.55 | - |
| Velocity | - | 0.36 | - | 0.37 | - | 0.38 | - |
| Drag | 26.46 | 27.1 | 2.42% | 28.14 | 6.35% | 30.5 | 15.27% |

are still smaller than 6 DOF conditions. Increasing the forward speed reduces the pitch and sway motions, and subsequently, their contribution on the maximum roll angle. The contribution of different motions at Froude number 0.1 and 0.19 are similar as shown in Figure 4, while the model at 6DOF still experiences larger roll angle.

When the phase shift between the exciting moment and roll angle is near to 90 degrees, the model experiences larger roll motion. Increasing the forward speed reduces the phase shift (Figure 4). Hence, the roll motion characteristics decrease for the higher froude numbers. Although, the fully appended model free in 6 DOF experiences larger phase shift compared to the bare hull model and closer to 90 degrees, it generates smaller roll motion characteristics. Because the appendages create a moment to resist development of the roll angle. For the model free in roll and sway (RS) there is a smaller phase shift compared to the other DOF conditions. On the other hand, the coupled roll-pitch (RP) motion has larger phase shift.

As shown in Figure 5 and Figure 6 the angular velocity and acceleration of the models under the same roll exciting moment are identical for the first cycle at different forward speeds. However, in the following cycles, where both amplitudes increase, rising the forward speed decreases the amplitude of angular velocity and acceleration. It is also shown that the reduction at higher speed is more significant. The bare and fully appended models free in 6 DOF have larger angular velocity and acceleration compared to the other cases. The model free in coupled roll-pitch (RP) and coupled roll-sway (RS) generate larger angular velocity and acceleration compared to the model free in a single roll and the coupled roll-heave (RH) conditions. The roll moment is a function of acceleration and varies in different cycles according to the angular acceleration. The effects of DOF on the roll moment are shown in Figure 7. The amplitude of the roll moment varies about 20 percent from the single to 6DOF conditions. Decreasing the DOF decreases the amplitude of roll motion characteristics. Therefore, the simulation results are underestimated and cannot be applied for a real sea condition. It makes inevitable to extend our investigation up to 6DOF.

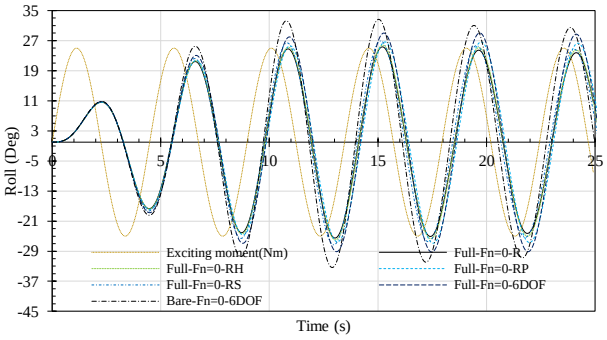


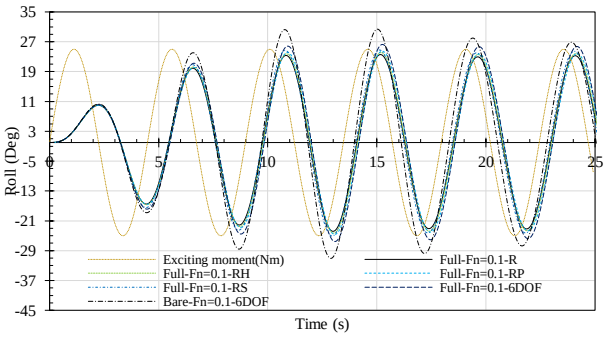

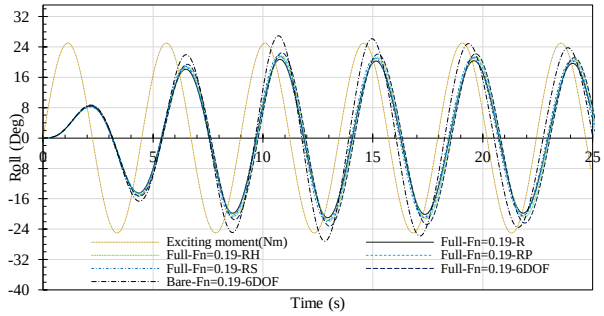


Figure 4 The roll angle trajectory under 25 Nm exciting moment at a frequency of 1.4 Rad/s, different Froude numbers (Fn.) and DOF.

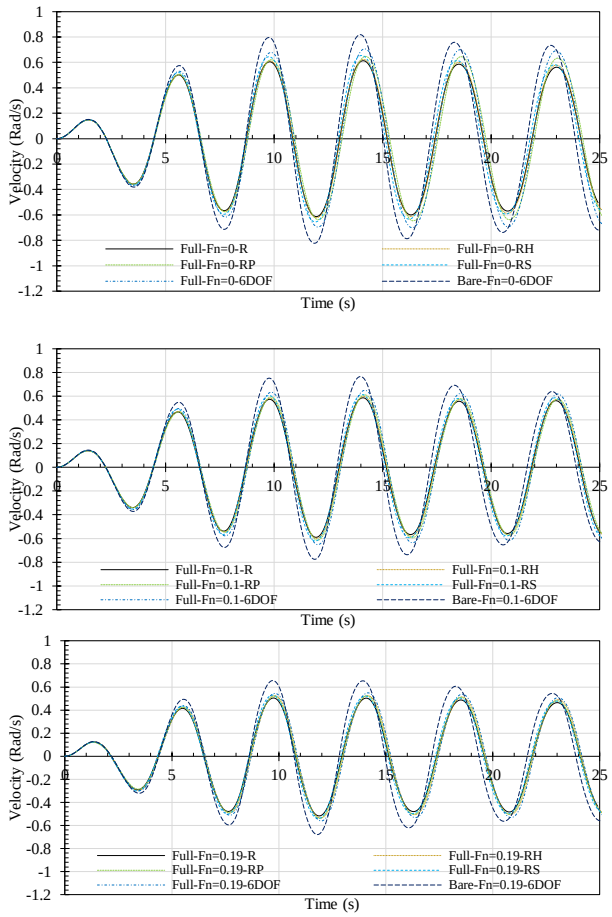


Figure 5 The angular velocity trajectory under 25 Nm exciting moment at a frequency of 1.4 Rad/s, different Froude numbers (Fn.) and DOF.

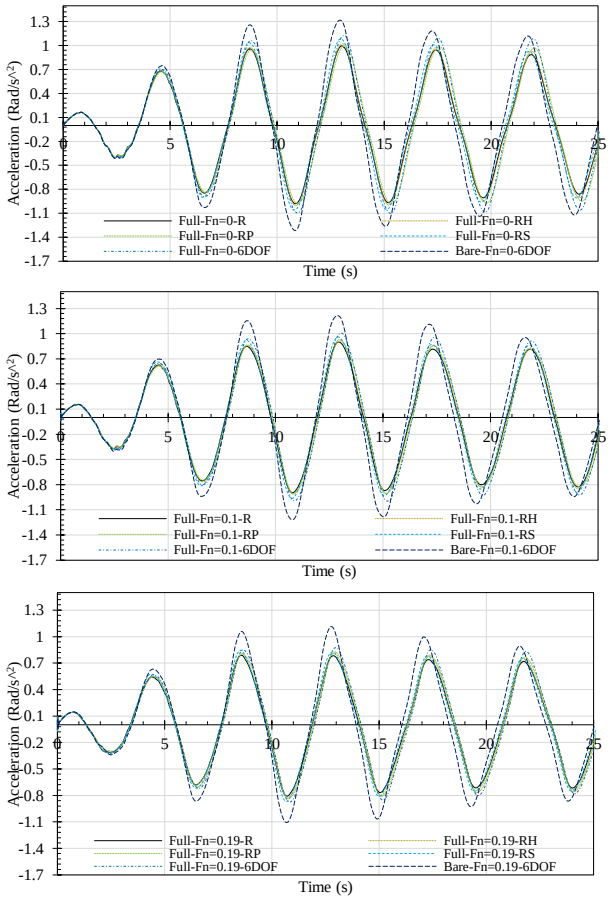


Figure 6 The angular acceleration trajectory under 25 Nm exciting moment at a frequency of 1.4 Rad/s, different Froude numbers (Fn.) and DOF.

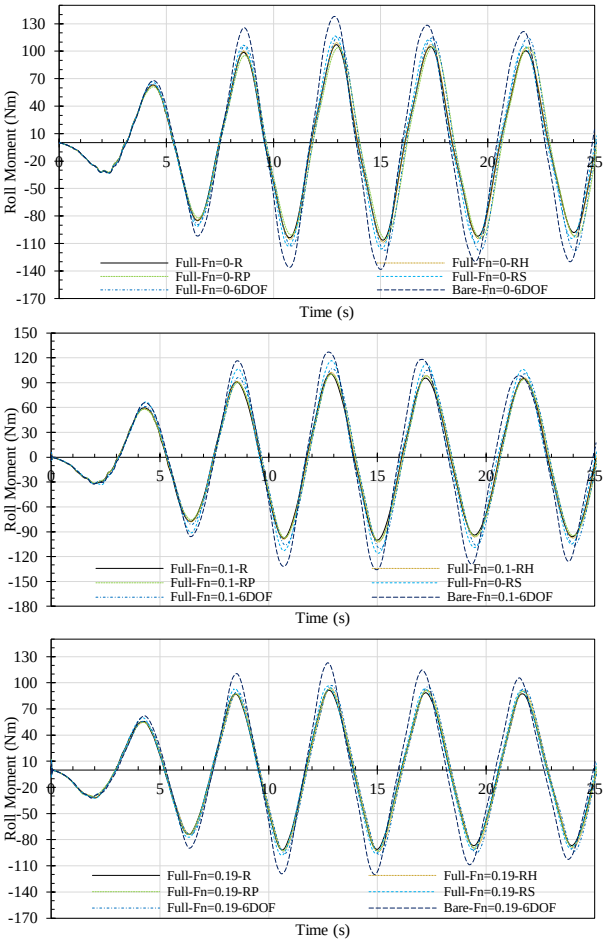


Figure 7 The roll moment trajectory under 25 Nm exciting moment at a frequency of 1.4 Rad/s, different Froude numbers (Fn.) and DOF.

## 4.2 Flow visualisation

Variation of vorticity magnitude in the middle section of the bare and fully appended models considering free in 6DOF at different forward speed are presented in Figure 8. The contours are recorded at about zero angle because the angular velocity and associated vorticity is in the maximum condition. It can be seen that at zero forward speed, the bilge keels generate larger vorticity compared to the bare hull model and changes the pressure distribution between two sides of the hull. Increasing the forward speed expands the vorticity along and across the hull. However, the magnitude of vorticity for the fully appended model is still larger than the bare hull. It means, the pressure differences between two sides of the fully appended model is larger at higher Froude numbers.

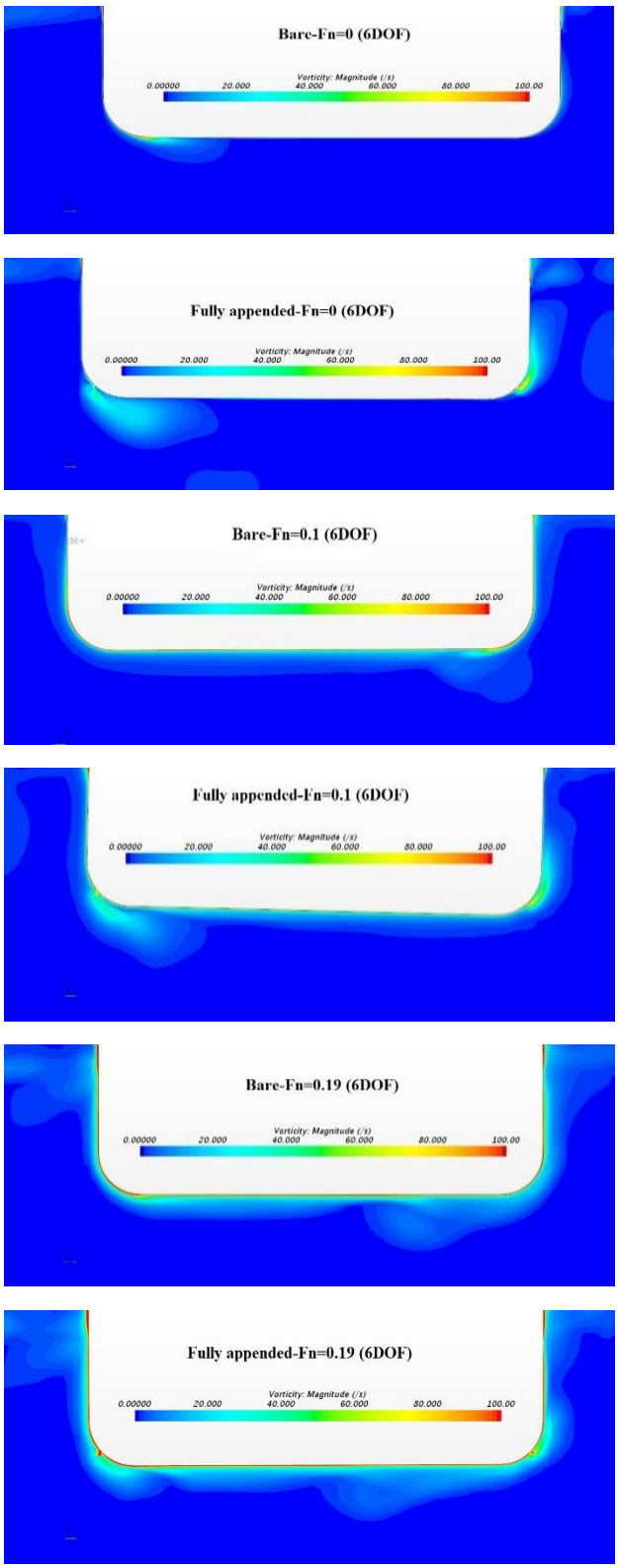


Figure 8 Comparison of the vorticity magnitude for the bare and fully appended models at different Froude numbers.

### 4.3 Magnitude of the roll inertia, damping and restoring moments

Variation of the mass and added mass moment of inertia, damping and restoring moments over different roll angles for both bare and fully appended models at different forward speeds and DOF are shown in Figure 9. The amplitude of exciting moment was 25 Nm at a frequency of 1.4 Rad/s. The negative sign was considered for the roll exciting moment and total mass moment of inertia (mass and added mass moment of inertia) because they collaborate to increase the roll motion and decrease the ship safety. On the other hand, the positive sign was considered for damping and restoring moment which oppose the roll motion development. The restoring moment has the largest value in all conditions. The mass moment of inertia has the second larger magnitude greater than the added moment of inertia. The damping moment has the smallest value, but it is an important parameter at a resonance frequency to counteract the roll motion increment. At the same time, there is a close interdependence between moments.

At the zero forward speed, the magnitude of dynamic restoring moment is larger than the static restoring moment at small roll angles due to the larger angular velocity and added dynamic pressure. Under the same exciting moment, the bare-hull model free in 6DOF experiences a larger virtual mass moment of inertia compared to the fully appended model, while it has smaller damping and restoring moments. Because the appendages by creating separation, increases the vorticity and reduces the acceleration or deceleration of fluid during roll motion (Figure 8). The appendages also generate a moment in opposite direction of the roll motion, causing the maximum roll angle to decrease. The coupled roll-pitch (RP) condition generates a larger damping and virtual moment of inertia due to the larger phase shift, while, the restoring moment remains smaller than the other DOF. The coupled roll-sway (RS) has the smaller damping moment with large restoring and virtual moment of inertia due to the smallest phase shift. It can be seen in Figure 9 that constraining the model free in 1 and 2 DOF reduces the magnitude of virtual mass moment of inertia significantly while increases the damping moment. On the other hand, the magnitude of restoring moment decreases slightly. Therefore, the magnitude of the contributor moments to increase the roll angle were declined and model in lower DOF experiences smaller roll motion characteristics.

The magnitude of restoring moment at higher speed for the small roll angle is relatively smaller than the zero forward speed conditions. Because the incoming flow reduces the pressure difference between two sides of the model. On the other hand, the magnitude of restoring moment at higher speed for the larger roll angles is relatively larger than the zero forward speed condition. The main reason of increase in pressure difference is due to the speed of flow which extend the separation and vorticities along the model. As can be seen from Figure 9, increasing forward speed increases the damping moment and reduces the virtual moment of inertia. The reduction in added moment of inertia at higher Froude number is significant and as result, the model experiences smaller roll motion. By increasing forward speed, the magnitude of virtual moment of inertia and damping moment varies for different DOF conditions. The coupled roll-heave (RH) has the larger damping and virtual moment of inertia. The results show that the restoring moment and damping moment for the fully appended model free in 6DOF at higher Froude number is larger than the bare hull model, while, the fully appended model has smaller virtual moment of inertia.

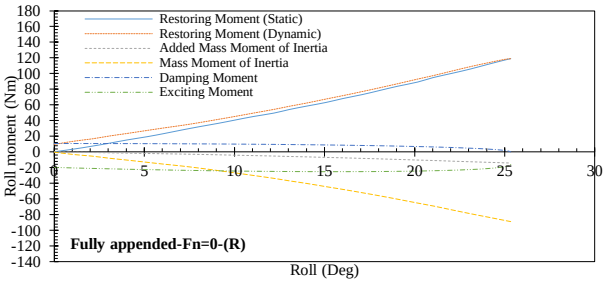
Restoring Moment (Static)
Restoring Moment (Dynamic)
Added Mass Moment of Inertia
Mass Moment of Inertia
Damping Moment
Exciting Moment
Roll moment (Nm)
Roll (Deg)
Fully appended-Fn=0-(R)

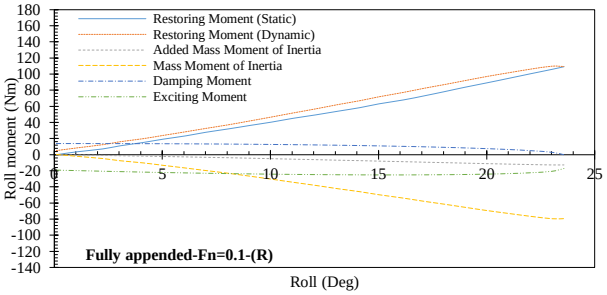
Restoring Moment (Static)
Restoring Moment (Dynamic)
Added Mass Moment of Inertia
Mass Moment of Inertia
Damping Moment
Exciting Moment
Roll moment (Nm)
Roll (Deg)
Fully appended-Fn=0.1-(R)

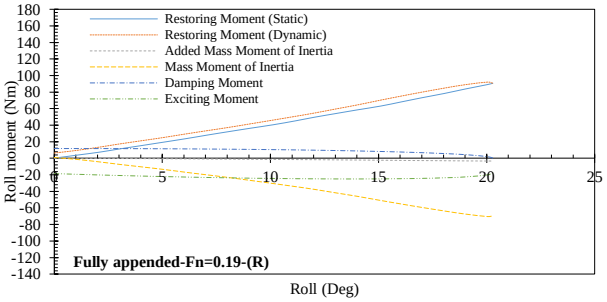
Restoring Moment (Static)
Restoring Moment (Dynamic)
Added Mass Moment of Inertia
Mass Moment of Inertia
Damping Moment
Exciting Moment
Roll moment (Nm)
Roll (Deg)
Fully appended-Fn=0.19-(R)

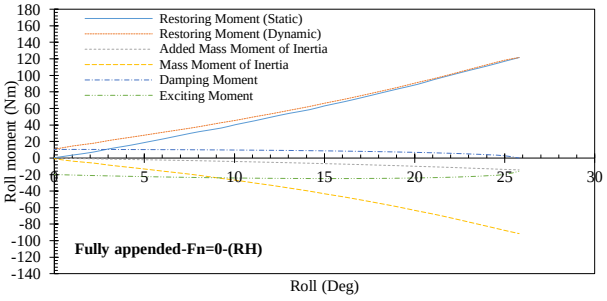
Restoring Moment (Static)
Restoring Moment (Dynamic)
Added Mass Moment of Inertia
Mass Moment of Inertia
Damping Moment
Exciting Moment
Roll moment (Nm)
Roll (Deg)
Fully appended-Fn=0-(RH)

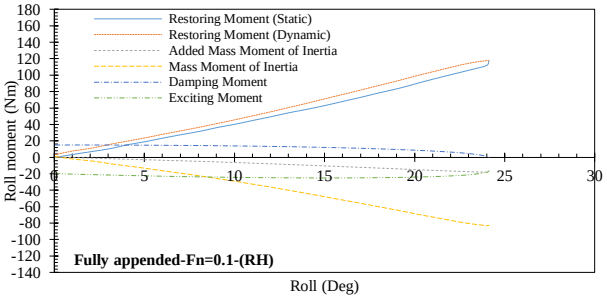
Restoring Moment (Static)
Restoring Moment (Dynamic)
Added Mass Moment of Inertia
Mass Moment of Inertia
Damping Moment
Exciting Moment
Roll moment (Nm)
Roll (Deg)
Fully appended-Fn=0.1-(RH)

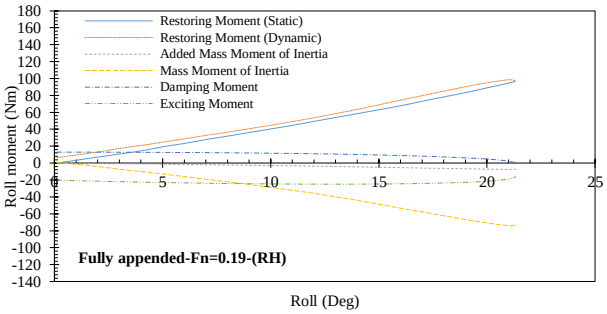
Restoring Moment (Static)
Restoring Moment (Dynamic)
Added Mass Moment of Inertia
Mass Moment of Inertia
Damping Moment
Exciting Moment
Roll moment (Nm)
Roll (Deg)
Fully appended-Fn=0.19-(RH)

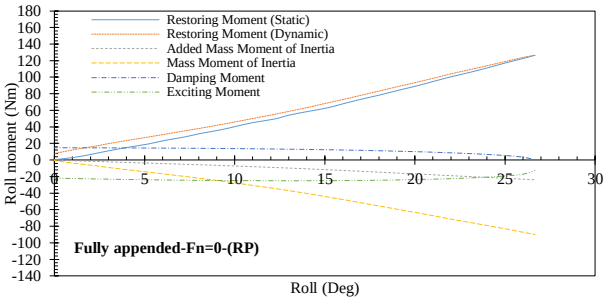
Restoring Moment (Static)
Restoring Moment (Dynamic)
Added Mass Moment of Inertia
Mass Moment of Inertia
Damping Moment
Exciting Moment
Roll moment (Nm)
Roll (Deg)
Fully appended-Fn=0-(RP)

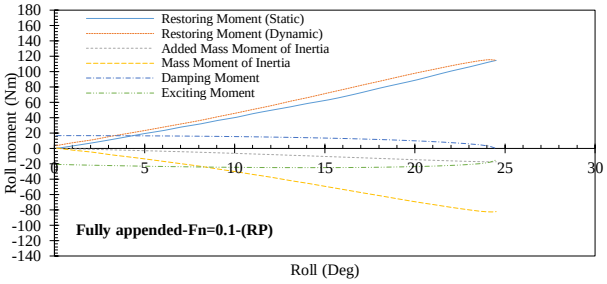
Restoring Moment (Static)
Restoring Moment (Dynamic)
Added Mass Moment of Inertia
Mass Moment of Inertia
Damping Moment
Exciting Moment
Roll moment (Nm)
Roll (Deg)
Fully appended-Fn=0.1-(RP)

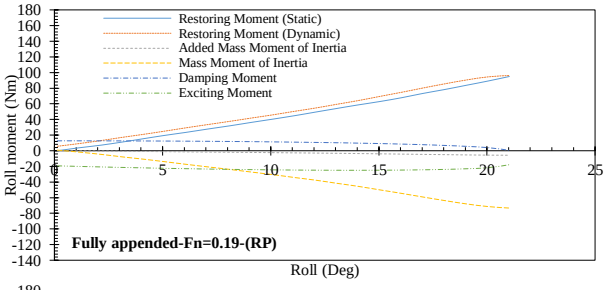
Restoring Moment (Static)
Restoring Moment (Dynamic)
Added Mass Moment of Inertia
Mass Moment of Inertia
Damping Moment
Exciting Moment
Roll moment (Nm)
Roll (Deg)
Fully appended-Fn=0.19-(RP)

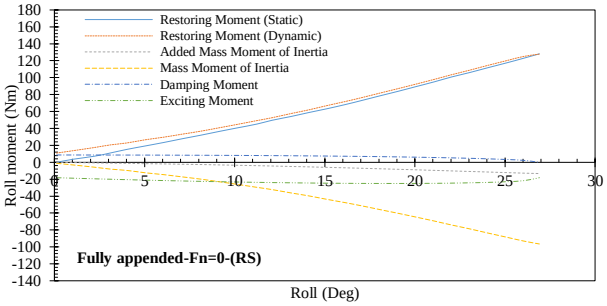
Restoring Moment (Static)
Restoring Moment (Dynamic)
Added Mass Moment of Inertia
Mass Moment of Inertia
Damping Moment
Exciting Moment
Roll moment (Nm)
Roll (Deg)
Fully appended-Fn=0-(RS)

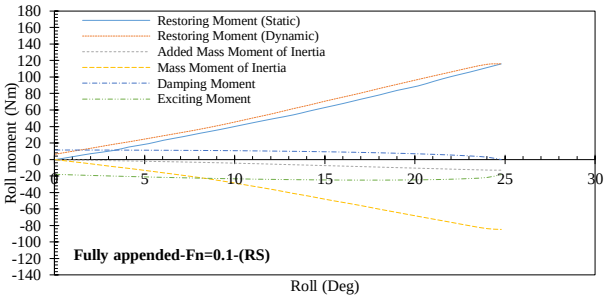
Restoring Moment (Static)
Restoring Moment (Dynamic)
Added Mass Moment of Inertia
Mass Moment of Inertia
Damping Moment
Exciting Moment
Roll moment (Nm)
Roll (Deg)
Fully appended-Fn=0.1-(RS)

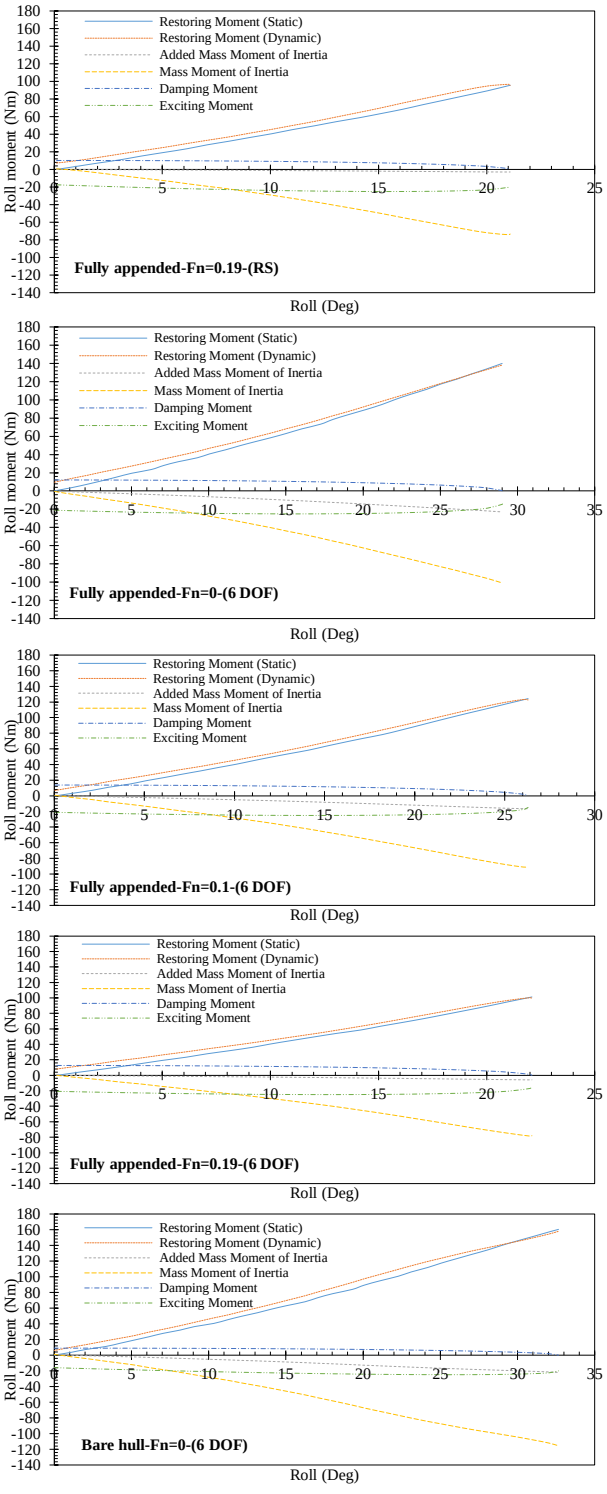


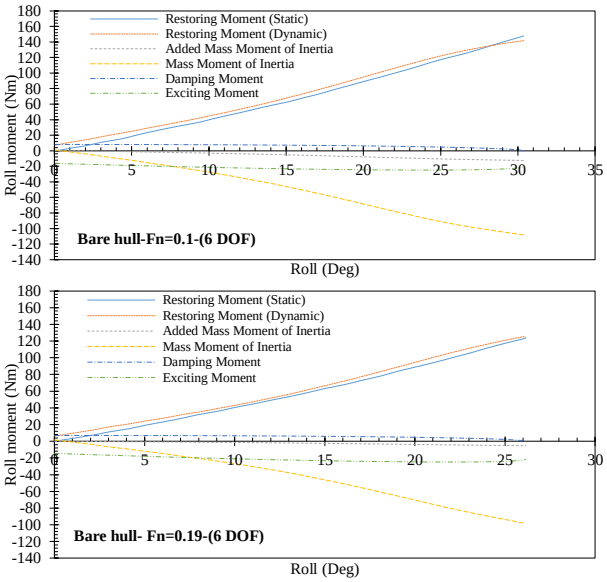





Figure 9 The variation of different roll moments versus the roll angle under 25 Nm exciting moment at a frequency of 1.4 Rad/s, bare and fully appended models, different Froude numbers and DOF conditions.

## 5. CONCLUDING REMARKS

CFD simulations were carried out to study the roll motion characteristics and to calculate the restoring moment over different roll angles in dynamic conditions. It was found that the appendages reduce the peak values of the motion characteristics, while they increase the phase shift between the exciting moment and roll trajectory. Increasing the forward speed reduces both maximum roll angle and phase shift. Decreasing the DOF decreases the motion characteristics.

The computed restoring moment in dynamic condition was larger than the static condition. That is especially about small roll angle, due to the angular velocity being at a highest value and dynamic pressure adds up to the hydrostatic pressure. The appendages increase the pressure difference between two sides of the model by generating the vorticity, therefore, the restoring moment of the fully appended condition is larger than the bare hull condition. Increasing DOF increases the magnitude of restoring

moment and the sway motion specifically has the greater contribution among other motions.

Increasing the Froude number increases the damping moment while reduces the added moment of inertia. The reduction of added moment of inertia is considerable at the highest Froude number, which is the main reason for smaller roll angle.

## 6. REFERENCES


BULIAN, G., FRANCESCUTTO, A., and LUGNI, C., 2006, "Theoretical, numerical and experimental study on the problem of ergodicity and 'practical ergodicity'with an application to parametric roll in longitudinal long crested irregular sea" Ocean engineering, 33**,** 1007-1043.

DUNWOODY, A. B., 1989, "ROLL OF A SHIP IN ASTERN SEAS--METACENTRIC HEIGHT SPECTRA", Journal of ship research, 33.

FERZIGER, J. H., PERIC, M., and LEONARD, A., 1997, "Computational methods for fluid dynamics", AIP.

FIELD, P. L., 2013, "Comparison of RANS and Potential Flow Force Computations for the ONR Tumblehome Hullfrom in Vertical Plane Radiation and Diffraction Problems", Virginia Tech.

HANDSCHEL, S. and ABDEL-MAKSOUD, M., 2014, "Improvement of the Harmonic Excited Roll Motion Technique for Estimating Roll Damping", Ship Technology Research, 61**,** 116-130.

HOLDEN, C., GALEAZZI, R., RODRÍGUEZ, C., PEREZ, T., FOSSEN, T. I., BLANKE, M., and DE ALMEIDA SANTOS NEVES, M., 2007, "Nonlinear container ship model for the study of parametric roll resonance", Modeling, identification and control, 28**,** 87-103.

KIANEJAD, S., ENSHAEI, H., and RANMUTHUGALA, D., 2017, "Estimation of added mass moment of inertia in roll motion through numerical simulation", PACIFIC 2017 International Maritime Conference, 1-15.

MOCTAR, O. E., SHIGUNOV, V., and ZORN, T., 2012, "Duisburg Test Case: Post-panamax container ship for benchmarking", Ship Technology Research, 59**,** 50-64.

NEVES, M. A., 2002, "On the excitation of combination modes associated with parametric resonance in waves", Proceedings of the 6th International Ship Stability Workshop.

NEVES, M. A., PÉREZ, N., and LORCA, O., 2002, "Experimental analysis on parametric resonance for two fishing vessels in head seas", Proceedings of the 6th International Ship Stability Workshop.

OH, I., NAYFEH, A. and MOOK, D., 2000, "A theoretical and experimental investigation of indirectly excited roll motion in ships", Philosophical Transactions of the Royal Society of London A: Mathematical, Physical and Engineering Sciences, 358**,** 1853-1881.

SILVA, S., SANTOS, T., and SOARES, C. G., 2005, "Parametrically excited roll in regular and irregular head seas", International Shipbuilding Progress, 52**,** 29-56.

SIMONSEN, C. D., OTZEN, J. F., JONCQUEZ, S., and STERN, F., 2013, "EFD and CFD for KCS heaving and pitching in regular head waves", Journal of Marine Science and Technology, 18**,** 435-459.

SONG, K.-H., KIM, Y., and PARK, D.-M., 2013, "Quantitative and qualitative analyses of parametric roll for ship design and operational guidance", Proceedings of the Institution of Mechanical Engineers, Part M: Journal of Engineering for the Maritime Environment, 227**,** 177-189.

TEZDOGAN, T., DEMIREL, Y. K., KELLETT, P., KHORASANCHI, M., INCECIK, A., and TURAN, O., 2015, "Full-scale unsteady RANS CFD simulations of ship behaviour and performance in head seas due to slow steaming", Ocean Engineering, 97**,** 186-206.

VIDIC-PERUNOVIC, J., 2011, "Influence of the GZ calculation method on parametric roll prediction", Ocean Engineering, 38**,** 295-303.

WAWRZYŃSKI, W. and KRATA, P., 2016, "On ship roll resonance frequency", Ocean Engineering, 126**,** 92-114.